Bayesian framework for elastic full-waveform inversion with facies information

Sagar Singh[1], Ilya Tsvankin[1], and Ehsan Zahibi Naeini[2]

https://doi.org/10.1190/tle37120924.1.

Abstract

Conventional reservoir-characterization techniques utilize amplitude-variation-with-offset (AVO) analysis to invert for the elastic parameters or directly for the physical properties of reservoirs. However, the quality of AVO inversion is degraded by errors in the velocity model, inaccurate amplitudes, and structural complexity. Whereas full-waveform inversion (FWI) potentially represents a much more powerful tool for reservoir characterization. FWI strongly relies on the accuracy of the initial model and suffers from parameters trade-offs. Here, we use a probabilistic Bayesian framework to supplement data fitting with rock-physics constraints based on geologic facies obtained from borehole information (well logs). The advantages of the facies-based FWI are demonstrated on a structurally complex isotropic elastic model and on a 3D layered VTI (transversely isotropic with a vertical symmetry axis) medium. In particular, the tests show that our algorithm can operate without ultra-low-frequency data required by conventional FWI and can reduce crosstalk between the medium parameters.

Introduction

Amplitude-variation-with-offset (AVO) analysis remains the most common tool for estimation of reservoir properties from seismic data (Buland and Omre, 2003; Coléou et al., 2005; Saussas and Sams, 2012; Grana, 2016; Zabihi Naeini and Exley, 2017). Elastic parameters or reservoir properties can be evaluated by deterministic or stochastic inversion of the AVO response (e.g., Russell, 1988). Conventional algorithms usually generate a reservoir model by iteratively reducing the difference between migrated data and synthetic traces generated using petroelastic information. Saussus and Sams (2012) employ geologic facies to constrain this inversion workflow, which yields a more plausible reservoir description. However, as discussed by Zabihi Naeini et al. (2016), the AVO-based approach suffers from such inherent problems as high sensitivity to velocity errors and distortions due to model complexity. Also, AVO analysis operates only with the amplitudes of reflected waves.

Full-waveform inversion (FWI) has been successfully used for building high-resolution velocity models that improve seismic images (Tarantola, 1984; Virieux and Operto, 2009) and could be applied to characterization of petroleum reservoirs (Zabihi Naeini et al., 2016). However, computational demands for large-scale implementation of such a method are yet to be evaluated. Despite the potential advantages of FWI over conventional reservoir-characterization methods, waveform inversion involves a number of challenges. In the absence of low frequencies in the recorded data, FWI often fails to converge to the global minimum if the initial model is not sufficiently accurate. Parameter trade-offs, even in a purely isotropic acoustic medium, can lead to substantial parameter distortions (Operto et al., 2013; Alkhalifah and Plessix, 2014; Oh and Alkhalifah, 2016). One option to reduce such trade-offs without relying on ultra-low frequencies is to supplement the FWI workflow with prior model constraints based on geologic facies (commonly derived from well logs).

To incorporate facies-based rock-physics constraints, one has to know the spatial distribution of the facies. Attempts to make FWI more robust by including a facies distribution have shown some promise (Zhang et al., 2017). In particular, Kamath et al. (2017) use a two-stage process to incorporate facies information into FWI. The results of the conventional FWI (first inversion stage) are employed to build the facies which are compared to the prior facies model obtained from a well log. Each grid point in the model is assigned to one of the facies depending on the match between the synthetic and actual facies distribution, thereby yielding constraints for the second inversion stage. Zhang et al. (2017) determine the spatial distribution of the facies by calculating at each grid point the maximum posterior probability of the inverted parameter for all facies in the prior model. Both techniques operate with relatively simple layered media that have mild lateral heterogeneity. Because Kamath et al. (2017) incorporate information from a single borehole, the wrong facies can be assigned to certain grid points if the model is structurally complicated with pronounced lateral gradients. For the same reason, the inversion results of Zhang et al. (2017) include artifacts (e.g., edge effects).

To make the facies analysis more robust, Zhang et al. (2018) employ P-wave radiation patterns to determine the subsurface regions where each parameter is well constrained by the recorded data. When calculating the facies map, a more significant weight is assigned to the parameter that has a smaller uncertainty, which yields a modified map. Although this technique enhances resolution for structurally complicated media, it relies on the high accuracy of the initial model.

Considering all facies present in the model should provide higher resolution compared to that for a single-facies relationship between the elastic parameters for the entire section (Kemper and Gunning, 2014; Zabihi Naeini and Exley, 2017). After constructing the initial (prior) facies model, we use a probabilistic approach based on the Bayesian framework to estimate the "confidence model" that contains the spatial distribution of the facies. The confidence model is updated at each iteration and employed as a constraint in the inversion workflow. The update depends on the distribution of the elastic parameters after the previous iteration. Implementing this technique for structurally

[1]Colorado School of Mines, Center for Wave Phenomena, Golden, Colorado, USA. E-mail: sagarsingh@mines.edu; ilya@mines.edu.
[2]Ikon Science, London, UK. E-mail: enaeini@ikonscience.com.

complex models is not straightforward. Building a sufficiently accurate a priori parameter distribution requires dense well coverage to properly account for lateral heterogeneity. To obtain the prior model for strongly heterogeneous media (e.g., for the isotropic Marmousi model mentioned later), we use multiple well logs, but they are still sparsely distributed in space. Therefore, our algorithm employs image-guided interpolation (Hale, 2010) to reconstruct the model parameters between the available boreholes. Because the 3D elastic VTI medium used in another example later has a simpler structure, the prior model for it is built by a technique similar to that of Kamath et al. (2017).

After describing the method, we apply it to the isotropic and VTI models mentioned earlier. The tests show that facies-based constraints can help recover a high-resolution model in the absence of ultra-low frequencies in the seismic data. Additionally, the initial model can significantly differ from the actual parameter distribution.

Theory

FWI is an iterative data-fitting technique that typically requires constraints to resolve the model parameters. Our objective function $\mathbf{E}(\mathbf{m})$ is based on the approach described by Zabihi Naeini et al. (2016), who discuss application of FWI as a reservoir-characterization tool (Figure 1):

$$\mathbf{E}(\mathbf{m}) = \mathbf{E}_{\mathrm{d}}(\mathbf{m}) + \beta \mathbf{E}_{\mathrm{prior}}(\mathbf{m}), \tag{1}$$

where

$$\mathbf{E}_{\mathrm{d}}(\mathbf{m}) = ||\mathbf{W}_{\mathrm{d}}(\mathbf{d}^{\mathrm{sim}} - \mathbf{d}^{\mathrm{obs}})||,$$
$$\mathbf{E}_{\mathrm{prior}}(\mathbf{m}) = ||\mathbf{W}_{\mathrm{m}}(\mathbf{m}_{\mathrm{inv}} - \mathbf{m}_{\mathrm{c}})||.$$

The term $\mathbf{E}_{\mathrm{d}}(\mathbf{m})$ represents the standard data-misfit l^2-norm, where $\mathbf{d}^{\mathrm{obs}}$ is the recorded seismic data, and $\mathbf{d}^{\mathrm{sim}}$ is the synthetic (simulated) data. The scaling matrices $\mathbf{W}_{\mathrm{d}}$ and $\mathbf{W}_{\mathrm{m}}$ are designed to make the data-fitting and prior-model terms dimensionless. The term $\beta \mathbf{E}_{\mathrm{prior}}(\mathbf{m})$ incorporates a priori rock-physics constraints based on the geologic facies; the vector $\mathbf{m}_{\mathrm{c}}$ represents the confidence model updated at each iteration, $\mathbf{m}_{\mathrm{inv}}$ is the inverted model, and β is a scaling factor.

Probabilistic approach based on the Bayesian framework is used to estimate the a priori spatial distribution of the facies. We compute the posterior probability of the facies as follows:

$$\mathrm{P}(\mathbf{f}|\mathbf{m}) = \frac{P(\mathbf{f}) \cdot \mathrm{P}(\mathbf{m}|\mathbf{f})}{\int \mathrm{P}(\mathbf{f}) \mathrm{P}(\mathbf{m}|\mathbf{f})}, \tag{2}$$

where $\mathbf{f}$ is the a priori facies vector, $\mathrm{P}(\mathbf{m}|\mathbf{f})$ is the likelihood function, and $\mathbf{m}$ represents the model obtained by the conventional FWI. A Gaussian distribution is used to describe the uncertainty in the model space (Tarantola, 1984):

$$\mathrm{P}(\mathbf{m}|\mathbf{f}) = \exp[-\gamma\,(\mathbf{m} - \mathbf{f}) \cdot (\mathbf{m} - \mathbf{f})], \tag{3}$$

where γ is the resolution parameter of the confidence model. The posterior probability is computed for each facies at all grid points

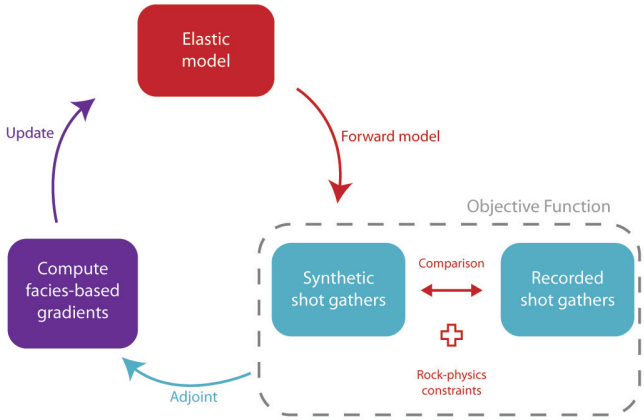

Figure 1. Flowchart for reservoir-oriented FWI with facies-based constraints (adapted from Zabihi Naeini et al., 2016).

of the model. The facies with the maximum posterior probability at a certain grid point determines the corresponding value in the confidence model.

The gradient of the data misfit with respect to the model parameters is obtained from the adjoint-state method (Plessix, 2006; Kamath and Tsvankin, 2016). For the isotropic Marmousi model below, iterative parameter updating is carried out with a multiscale approach using the bounded, low-memory Broyden-Fletcher-Goldfarb-Shanno algorithm of Byrd et al. (1995). For the 3D VTI example, the model is updated with the nonlinear conjugate-gradient algorithm (Hager and Zhang, 2006).

Accounting for lateral heterogeneity becomes highly challenging for complicated models such as Marmousi. Therefore, as mentioned earlier, in the elastic isotropic example we use multiple wells and build the prior model with image-guided interpolation based on the conventional reverse time migration (RTM) image, which is updated for each frequency band.

Numerical examples

Isotropic Marmousi model. The algorithm is first tested on the elastic isotropic Marmousi model (Martin et al., 2006), which is 10 km wide and 3.48 km thick (Figures 2a, 2c, and 2e). The modeling operator uses an 8$^{\mathrm{th}}$-order finite-difference scheme with PML boundary conditions to solve the elastic wave equation. The data are generated by 100 shots and recorded by 400 receivers, which are evenly distributed along the line and placed 40 and 80 m, respectively, beneath the surface. The input data are the vertical and horizontal particle velocities. The medium is parameterized by the P-wave (V_{P}) and S-wave (V_{S}) velocities and density (ρ). The algorithm is designed to invert for all three parameters using the inversion gradients presented by Köhn et al. (2012).

First, we conduct this test using a relatively accurate initial model obtained by smoothing the actual parameter distributions with a Gaussian function (Figures 2b, 2d, and 2f). The smoothing is designed to preserve the long-wavelength components of the actual model. Still, conventional (unconstrained) FWI requires low frequencies (down to 2 Hz) to reconstruct the medium parameters. We apply conventional FWI assuming that frequencies below 4 Hz are unavailable, which is usually the case in

practice; the inversion operates with four frequency bands (4–6, 4–10, 4–14, and 4–20 Hz). We follow the gradient preconditioning scheme described by Plessix and Mulder (2004) which compensates for amplitude decay due to geometric spreading. That allows us to define $\mathbf{W}_d$ in equation 1 as an identity matrix. The final inverted models (Figures 3a, 3c, and 3e) and parameter profiles (Figure 4) reveal the problems caused by the absence of low frequencies. The velocities V_P and V_S are distorted in the deeper part of the section, and errors in V_S are visible even up shallow. The estimated density also significantly deviates from the actual model.

To find out whether information about facies can compensate for the lack of low frequencies, we apply our facies-constrained algorithm for the same frequency range starting at 4 Hz. Rock-physics constraints are incorporated into the inversion workflow using the vertical parameter profiles ("well logs") at several locations along the line (Figure 5). The facies information for the well logs is obtained from Martin et al. (2006). Because the model is strongly heterogeneous, multiple well logs are required to produce a sufficiently detailed confidence model, which is created by image-guided interpolation. The high accuracy of the image obtained by conventional RTM makes it possible to define $\mathbf{W}_m$ in equation 1 as an identity matrix. (As mentioned earlier, $\mathbf{W}_d$ is an identity matrix as well.) In our implementation, the prior-model term in equation 1 is scaled by the factor β. For each inversion stage, β is gradually reduced with iterations, which improves convergence toward the actual model. Values of β for field-data applications should depend on the accuracy of the prior model and data quality.

The confidence models for all parameters are computed from the facies data using the Bayesian framework discussed earlier. The facies-based algorithm increases the spatial resolution (Figures 3b, 3d, and 3f) and estimates the model parameters with much higher accuracy than conventional FWI (Figure 4).

Next, we create initial parameter distributions which deviate further from the actual model compared with the previous test. The initial 1D model is generated from well-log data at location x = 0.8 km with mild smoothing in the vertical direction (Figures 6a–6c). This time, we assume that the lowest available frequency is 2 Hz rather than 4 Hz. Using the same frequency range as in the previous test (starting at 4 Hz) does not produce satisfactory results even with the facies-based constraints because the initial model is strongly distorted.

The conventional FWI is applied with a multiscale approach for the following frequency bands: 2–5, 2–8, 2–13, and 2–20 Hz. The final inversion results for the new initial model and set of frequency bands are shown in Figures 7a, 7c, and 7e and the vertical parameter profiles in Figure 8. Similar to the previous example, conventional FWI produces large errors in all three parameters, especially at depth. Supplementing the inversion workflow with facies-based constraints substantially improves the results (Figures 7b, 7d, and 7f). The superior performance of the facies-based FWI is particularly visible in the parameter profiles (Figure 8).

VTI model. The proposed technique was extended to VTI media parameterized by the P-wave and S-wave vertical velocities (V_{P0} and V_{S0}), the P-wave normal-moveout and horizontal velocities ($V_{nmo,P}$ and $V_{hor,P}$), and the SH-wave horizontal velocity ($V_{hor,SH}$) (Kamath and Tsvankin, 2016). Here, we present the

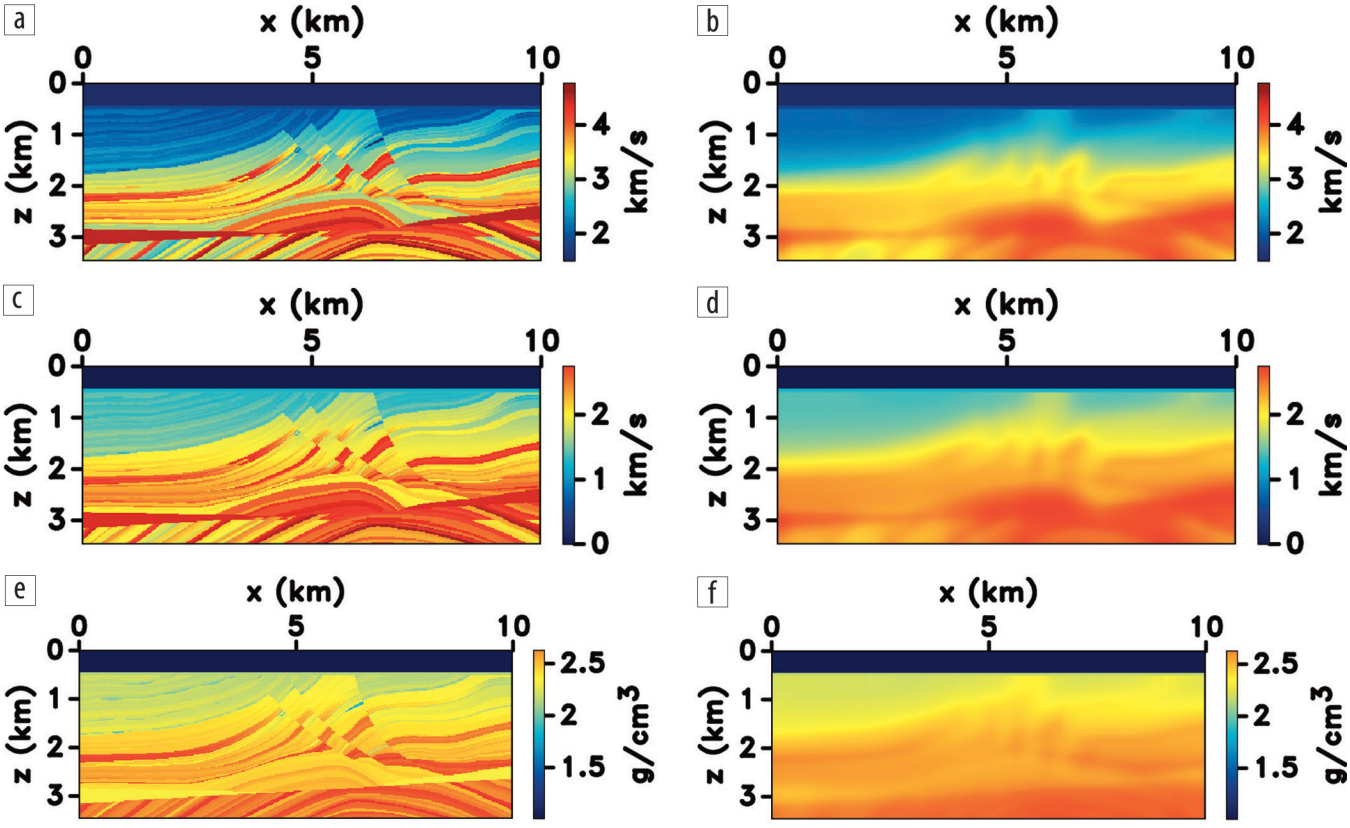

Figure 2. Parameters of the Marmousi model: (a) P-wave velocity (V_P), (c) S-wave velocity (V_S), and (e) density (ρ). Initial models of (b) V_P, (d) V_S, and (f) ρ.

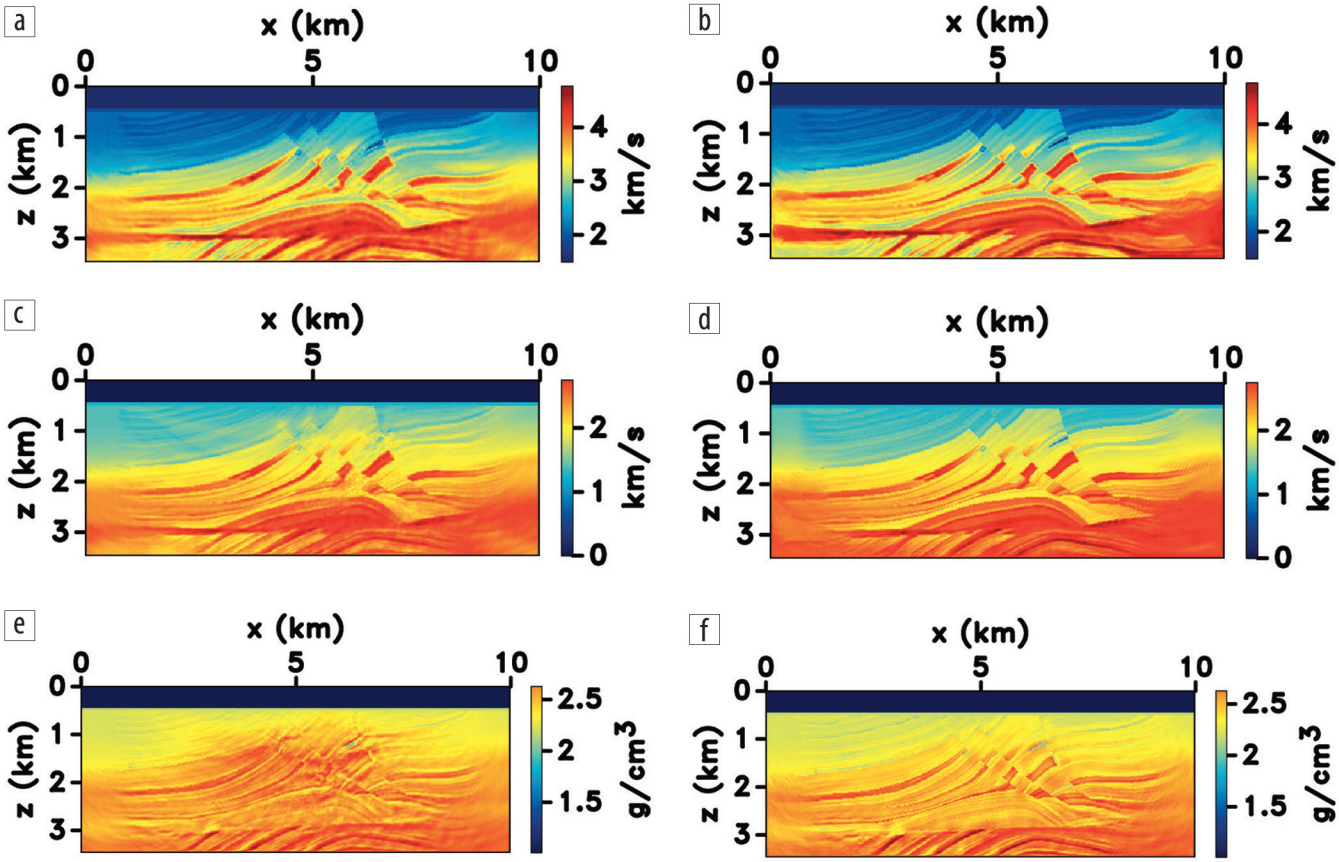

Figure 3. Results of the conventional FWI: (a) V_P, (c) V_S, and (e) ρ. The results of the facies-based FWI: (b) V_P, (d) V_S, and (f) ρ. The frequency range for the inversion is 4–20 Hz.

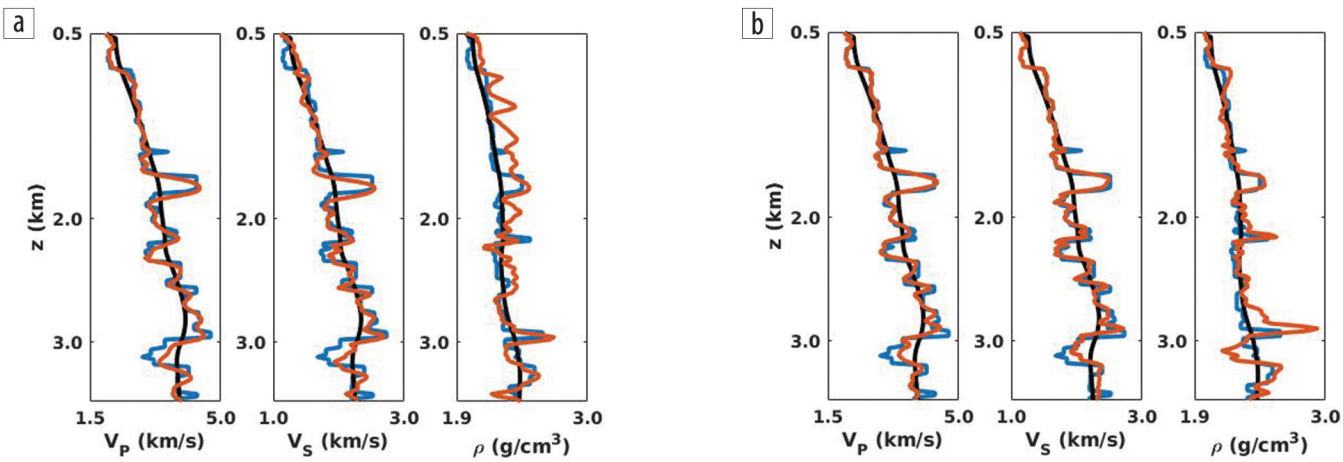

Figure 4. Vertical parameter profiles at x = 6 km: the actual (blue line), initial (black), and inverted (orange) parameters. The inversion is carried out by (a) conventional FWI and (b) facies-based FWI.

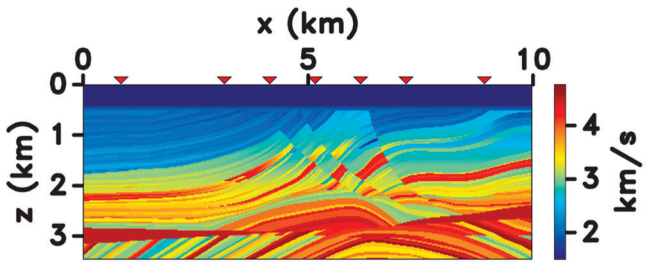

Figure 5. Locations of the well logs (red triangles) used for image-guided interpolation.

results of an initial test for a relatively simple 3D elastic VTI medium composed of coarse horizontal layers (Figure 9a). To simulate the wavefield, we extend to TI media a time-domain 3D elastic isotropic finite-difference modeling code, SOFI3D (Bohlen, 2002). Synthetic data are generated for a total of 100 sources and 2916 receivers, which are evenly distributed over the surface at a depth of 10 and 20 m, respectively. The density is kept constant throughout the model and is assumed known. The initial models represent smoothed versions of the actual parameter distributions that preserve the long-wavelength model components (Figure 9b).

We adapt and generalize for 3D the 2D time-domain inversion gradients for the parameterization from Kamath and Tsvankin (2016) that was mentioned earlier. To optimize memory usage, the gradients are computed from the frequency-domain forward and adjoint wavefield for several discrete frequencies. The discrete Fourier transform is applied to obtain the monochromatic wavefields for both forward and adjoint propagation. These wavefields are then cross-correlated and summed over all available discrete frequencies. Therefore, no storage of the time-domain wavefields at different time steps is required.

The conventional (unconstrained) inversion is applied with a multiscale approach using eight frequency bands in the range 4–20 Hz (the frequency increment is 0.3 Hz). Despite the simplicity of the structural model, the conventional method fails to produce a noticeable improvement in the resolution of the inverted parameters (Figures 9c and 10). In contrast, the facies-based

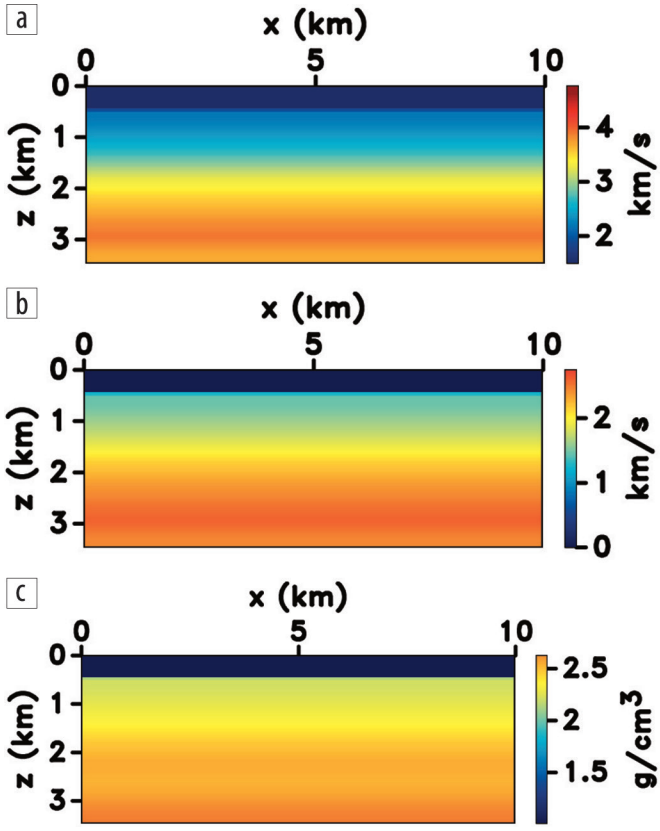

Figure 6. Initial parameters for the model in Figures 2a, 2b, and 2c: (a) V_P, (b) V_S, and (c) ρ.

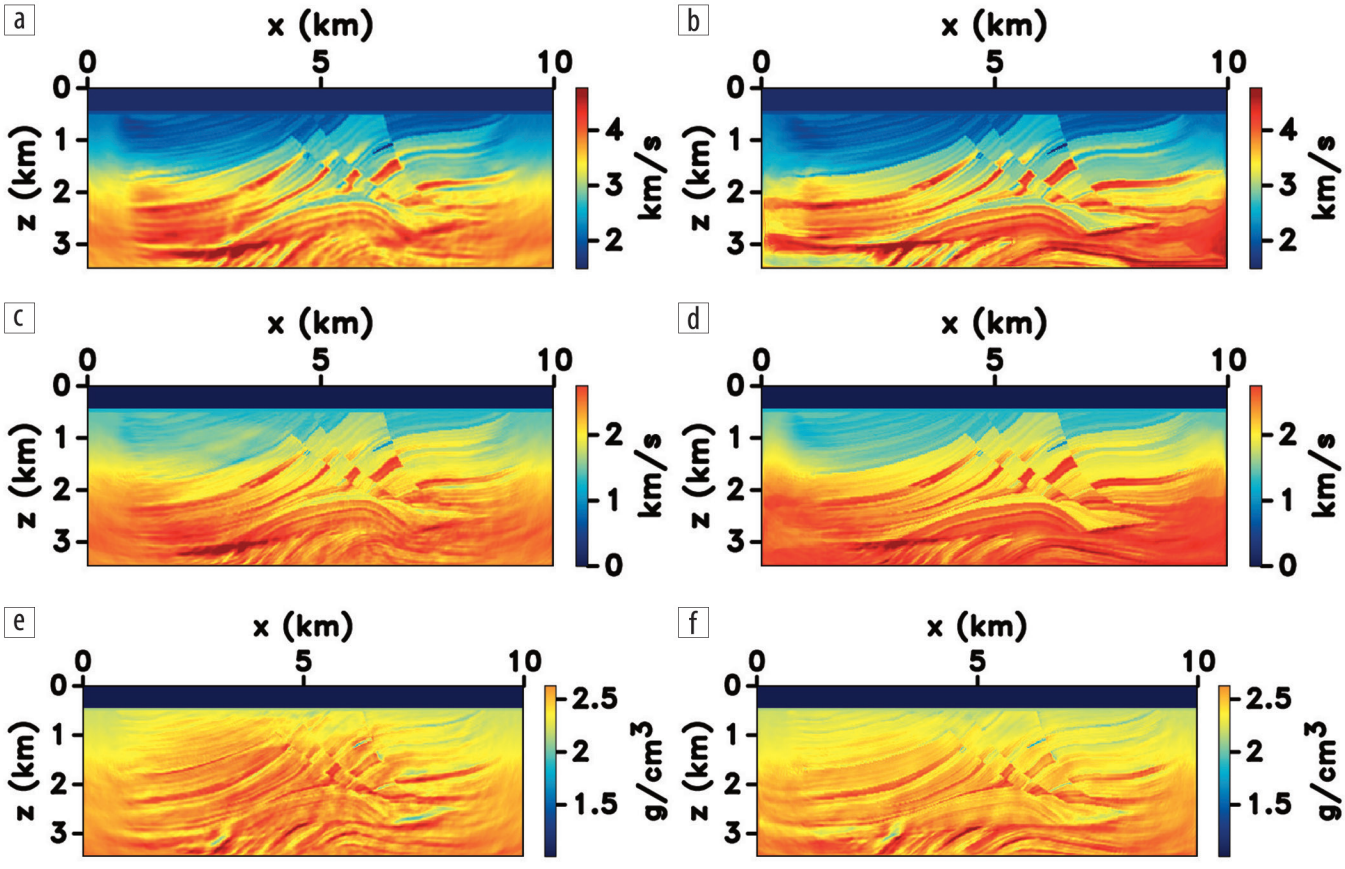

Figure 7. Inversion results for the initial model in Figure 6. Conventional FWI: (a) V_P, (c) V_S, and (e) ρ. Facies-based FWI: (b) V_P, (d) V_S, and (f) ρ. The frequency range is 2–20 Hz.

constraints result in proper parameter updates and help guide the algorithm toward the actual model (Figures 9d and 10).

Conclusions

We presented an efficient methodology for incorporating rock-physics constraints into the FWI workflow. A confidence model with the facies information, computed using the Bayesian framework, helps resolve the medium parameters with high spatial resolution. Synthetic tests on elastic isotropic and anisotropic models demonstrate the advantages of the facies-based FWI over the conventional algorithm and its potential as a reservoir-characterization tool. For the isotropic Marmousi model, the facies information was obtained from multiple well logs sparsely located in space. This information was employed in combination with image-guided interpolation to create the prior parameter distributions. The generated confidence model is updated at each iteration and used as a constraint in the FWI workflow. The algorithm was tested with two different frequency bands. For relatively accurate initial parameter distributions, the lowest frequency was set to 4 Hz, whereas for a more distorted initial model the lower bound of the frequency range was reduced to 2 Hz. The methodology was also extended to transversely isotropic media and applied to a 3D elastic VTI model parameterized by five velocities and density. In both tests, the

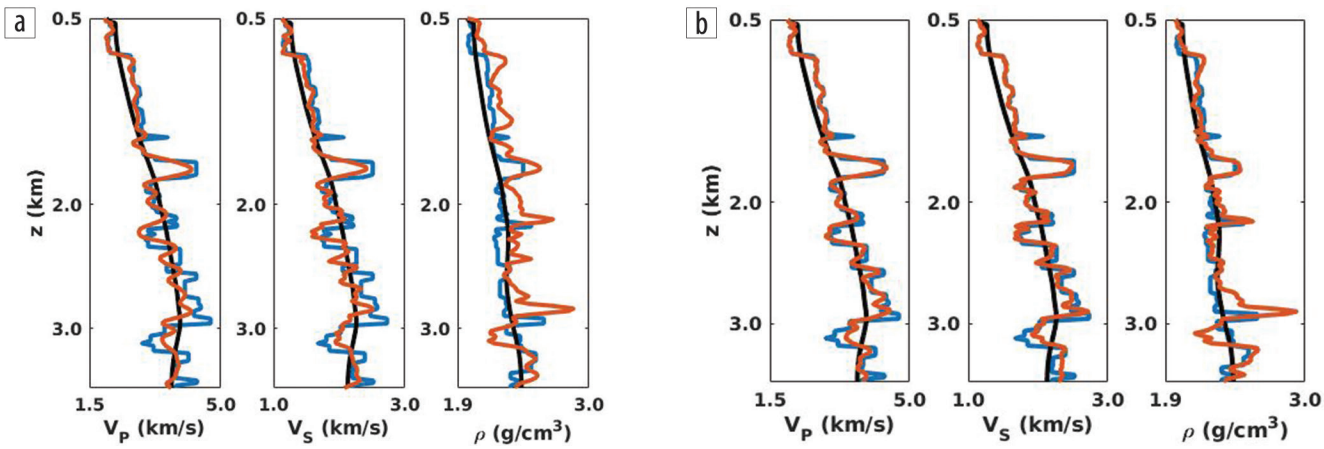

Figure 8. Vertical profiles at x = 6 km: the actual (blue line), initial (black), and inverted (orange) parameters. The inversion is carried out by (a) conventional FWI and (b) facies-based FWI with the initial model from Figure 6. The frequency range is 2–20 Hz.

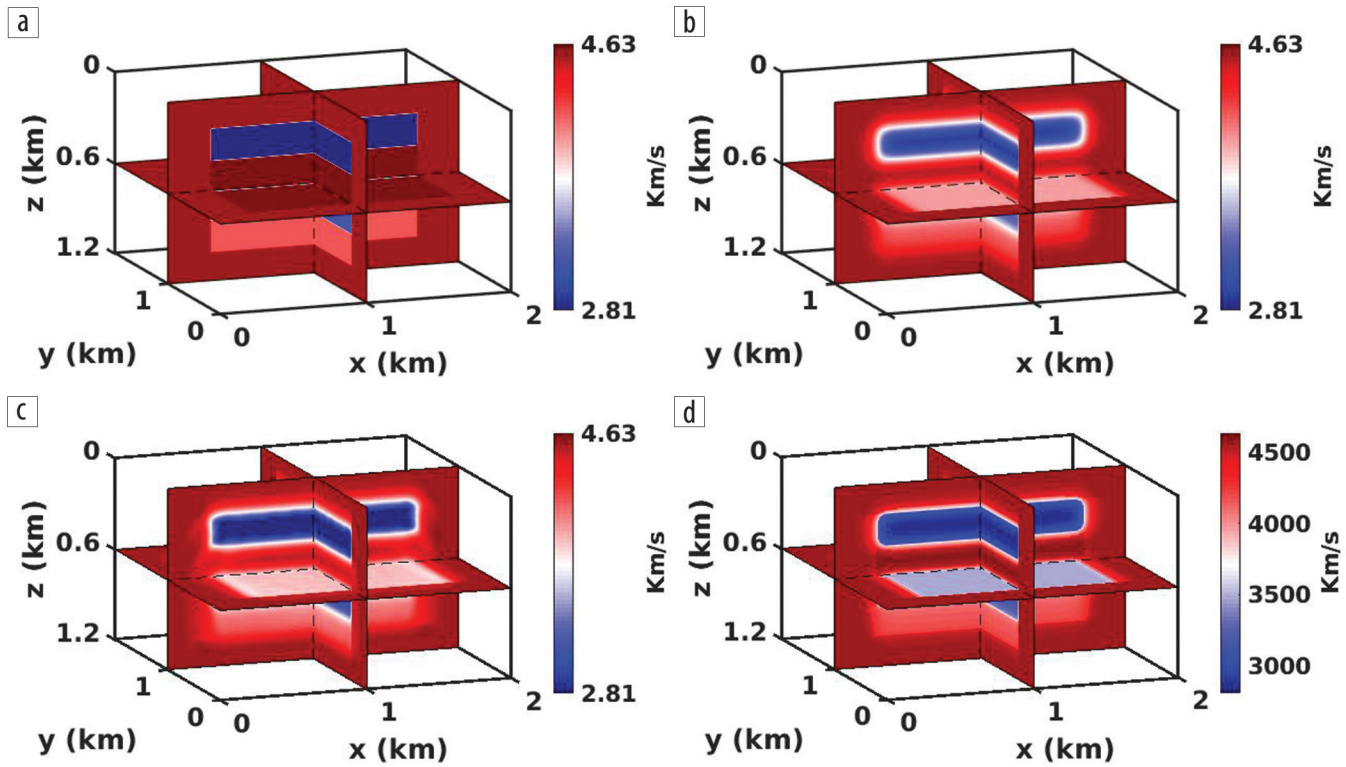

Figure 9. Actual (a) and initial (b) P-wave vertical velocity (V_{P0}) of a 3D elastic VTI model. The inverted V_{P0} obtained by (c) conventional FWI and (d) facies-based FWI.

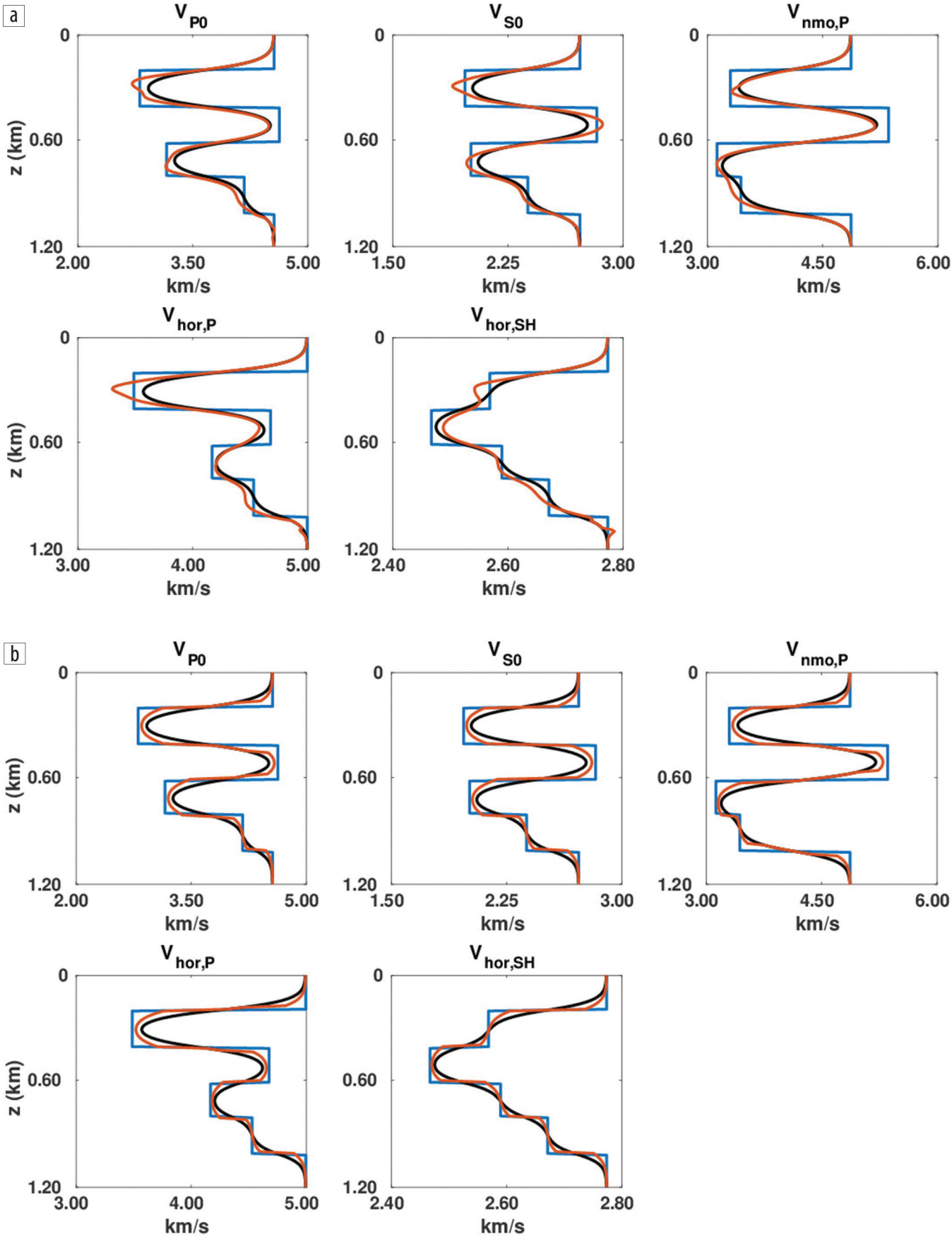

Figure 10. Vertical profiles at location x = y = 1 km: the actual (blue line), initial (black), and inverted (orange) parameters. The inversion is carried out by (a) conventional FWI and (b) facies-based FWI. The frequency range is 4–20 Hz.

facies-based FWI was able to mitigate parameter trade-offs that hamper conventional inversion and produce a high-resolution model without ultra-low frequencies in the data. TLE

Acknowledgments

We thank the members of the A(anisotropy)-Team at the Center for Wave Phenomena (CWP) for useful discussions. This work was supported by the Consortium Project on Seismic Inverse Methods for Complex Structures at the CWP and competitive research funding from King Abdullah University of Science and Technology.

Corresponding author: sagarsingh@mines.edu

References

Alkhalifah, T., and R. E. Plessix, 2014, A recipe for practical full-waveform inversion in anisotropic media: An analytical parameter resolution study: Geophysics, **79**, no. 3, R91–R101, https://doi.org/10.1190/geo2013-0366.1.

Bohlen, T., 2002, Parallel 3-D viscoelastic finite-difference seismic modelling: Computers & Geosciences, **28**, no. 8, 887–899, https://doi.org/10.1016/S0098-3004(02)00006-7.

Buland, A., and H. Omre, 2003, Bayesian linearized AVO inversion: Geophysics, **68**, no. 1, 185–198, https://doi.org/10.1190/1.1543206.

Byrd, R. H., P. Lu, J. Nocedal, and C. Zhu, 1995, A limited memory algorithm for bound constrained optimization: SIAM Journal on Scientific Computing, **16**, no. 5, 1190–1208, https://doi.org/10.1137/0916069.

Coléou, T., F. Allo, R. Bornard, J. Hamman, and D. Caldwell, 2005, Petrophysical seismic inversion: 75th Annual International Meeting, SEG, Expanded Abstracts, 1355–1358, https://doi.org/10.1190/1.2147938.

Grana, D., 2016, Bayesian linearized rock-physics inversion: Geophysics, **81**, no. 6, D625–D641, https://doi.org/10.1190/geo2016-0161.1.

Hager, W. W., and H. Zhang, 2006, A survey of nonlinear conjugate gradient methods: Pacific Journal of Optimization, **2**, no. 1, 35–58.

Hale, D., 2010, 2010, Image-guided 3D interpolation of borehole data: 80th Annual International Meeting, SEG, Expanded Abstracts, 1266–1270, https://doi.org/10.1190/1.3513074.

Kamath, N., and I. Tsvankin, 2016, Elastic full-waveform inversion for VTI media: Methodology and sensitivity analysis: Geophysics, **81**, no. 2, C53–C68, https://doi.org/10.1190/geo2014-0586.1.

Kamath, N., I. Tsvankin, and E. Zabihi Naeini, 2017, Facies-constrained FWI: Toward application to reservoir characterization: The Leading Edge, **36**, no. 11, 924–930, https://doi.org/10.1190/tle36110924.1.

Kemper, M., and J. Gunning, 2014, Joint impedance and facies inversion — Seismic inversion redefined: First Break, **32**, no. 9, 89–95.

Köhn, D., D. De Nil, A. Kurzmann, A. Przebindowska, and T. Bohlen, 2012, On the influence of model parametrization in elastic full waveform tomography: Geophysical Journal International, **191**, no. 1, 325–345, https://doi.org/10.1111/j.1365-246X.2012.05633.x.

Martin, G., R. Wiley, and K. J. Marfurt, 2006, Marmousi2: An elastic upgrade for Marmousi: The Leading Edge, **25**, no. 2, 156–166, https://doi.org/10.1190/1.2172306.

Oh, J.-W., and T. Alkhalifah, 2016, Elastic orthorhombic anisotropic parameter inversion: An analysis of parameterization: Geophysics, **81**, no. 6, C279–C293, https://doi.org/10.1190/geo2015-0656.1.

Operto, S., Y. Gholami, V. Prieux, A. Ribodetti, R. Brossier, L. Metivier, and J. Virieux, 2013, A guided tour of multiparameter full-waveform inversion with multicomponent data: From theory to practice: The Leading Edge, **32**, no. 9, 1040–1054, https://doi.org/10.1190/tle32091040.1.

Plessix, R.-E., 2006, A review of the adjoint-state method for computing the gradient of a functional with geophysical applications: Geophysical Journal International, **167**, no. 2, 495–503, https://doi.org/10.1111/j.1365-246X.2006.02978.x.

Plessix, R.-E., and W. A. Mulder, 2004, Frequency-domain finite-difference amplitude-preserving migration: Geophysical Journal International, **157**, no. 3, 975–987, https://doi.org/10.1111/j.1365-246X.2004.02282.x.

Russell, B. H., 1988, Introduction to seismic inversion methods: SEG, https://doi.org/10.1190/1.9781560802303.

Saussus, D., and M. Sams, 2012, Facies as the key to using seismic inversion for modelling reservoir properties: First Break, **30**, no. 7, 45–52.

Tarantola, A., 1984, Linearized inversion of seismic reflection data: Geophysical Prospecting, **32**, no. 6, 998–1015, https://doi.org/10.1111/j.1365-2478.1984.tb00751.x.

Virieux, J., and S. Operto, 2009, An overview of full-waveform inversion in exploration geophysics: Geophysics, **74**, no. 6, WCC1–WCC26, https://doi.org/10.1190/1.3238367.

Zabihi Naeini, E., and R. Exley, 2017, Quantitative interpretation using facies-based seismic inversion: Interpretation, **5**, no. 3, SL1–SL8, https://doi.org/10.1190/INT-2016-0178.1.

Zabihi Naeini, E., T. Alkhalifah, I. Tsvankin, N. Kamath, and J. Cheng, 2016, Main components of full-waveform inversion for reservoir characterization: First Break, **34**, no. 11, 37–48.

Zhang, Z., T. Alkhalifah, and E. Zabihi Naeini, 2017, Multiparameter elastic full waveform inversion with facies constraints: 87th Annual International Meeting, SEG, Expanded Abstracts, 1551–1555, https://doi.org/10.1190/segam2017-17672943.1.

Zhang, Z., T. Alkhalifah, E. Zabihi Naeini, and B. Sun, 2018, Multiparameter elastic full waveform inversion with facies-based constraints: Geophysical Journal International, **213**, no. 3, 2112–2127, https://doi.org/10.1093/gji/ggy113.